Aerodynamic and Aeroacoustic Numerical Investigation of Turbofan Engines using Lattice Boltzmann Methods

Thomas Hainaut, Thomas Le Garrec, Cyril Polacsek, Daniel Mincu, Sébastien Deck

Aerodynamic and Aeroacoustic Numerical Investigation of Turbofan Engines using Lattice Boltzmann Methods

Thomas Hainaut* and Thomas Le Garrec† and Cyril Polacsek‡ and Daniel Ciprian-Mincu§ and Sebastien Deck¶
The French Aerospace Lab ONERA, Chatillon Cedex, 92322, France

In recent years, lattice Boltzmann methods showed promising advantages over standard Navier-Stokes equation-based solvers, yet, their mesh structure is not ideal to computationally simulate the physics of turbulent boundary layers. In this work, with the objective of simulating turbomachine aerodynamics and aeroacoustics, a Delayed Detached Eddy Simulation using a Spalart-Allmaras turbulence model is performed in place of a standard sub-grid scale viscosity at the boundary layer. This approach is investigated on three benchmark cases, each focusing on challenging aspects of turbofan engines. Firstly, to assess the capability of self-noise generation, a symmetric aerofoil at high Reynolds number and at angle of attack is studied. Secondly, for leading edge noise predictions, a rod-aerofoil interaction noise case, where the rod generates a turbulence wake, which impinges the leading edge of the aerofoil. Finally, a case combining self-noise and interaction noise on mobile surfaces is investigated using a turbofan in rotation interacting with a grid-generated incoming turbulence.

I. Introduction

With the ever increasing air traffic and stricter noise regulations around airports, aircraft manufacturers require faster and more accurate numerical tools to allow for reliable aerodynamic and aeroacoustic investigations of complex systems. In recent years, Lattice Boltzmann Methods (LBM) proved efficient at simulating very large CFD problems on massively parallel clusters [1–5]. One advantage of LBM is its natural very low dissipative method, allowing for relatively small number of points per wavelength. However, one important drawback, which makes it strength on other aspects, is its lattice structure which is, in itself, not perfectly adapted to account for complex geometries and mesh turbulent boundary layers. To solves this first issue, immersed boundary conditions are commonly employed [1–3]. To address this second issue, a turbulence model is performed in this work. It relies on a Delayed Detached Eddy Simulation (DDES) [6] based on a Spalart-Allmaras turbulence model [7, 8]. This turbulence model has been historically introduced for RANS solvers with the objective of computing the Reynolds stresses, as the averaged equations are not closed. Based on the Boussinesq hypothesis which states that he momentum transfer caused by turbulent eddies can be modeled with an eddy viscosity ν_t, the Spalart-Allmaras model is a one transport equation for a viscosity-like variable, directly linked to the turbulent eddy viscosity ν_t [7, 8].

In this work, in the context of turbomachine aerodynamic and aeroacoustic numerical investigations, a turbulence modeling at solid boundaries using a DDES approach is performed on three benchmark cases. Firstly, to assess the capability of self-noise generation, a symmetric aerofoil at high Reynolds number and at angle of attack is studied. Secondly, for leading edge noise predictions, a rod-aerofoil interaction noise case, where the rod generates a turbulence wake, which impinges the leading edge of the aerofoil. Also, the complex physics associated with the turbulence generation in the wake of the rod as well as the aeroacoustics from both the back of the rod and the leading edge of the aerofoil makes it a comprehensive benchmark. Finally, a case combining self-noise and interaction noise on mobile surfaces is investigated using a turbofan in rotation interacting with a grid-generated incoming turbulence.

*Research Fellow, DAAA, thomas.hainaut@onera.fr.
†Research Engineer, DAAA, thomas.legarrec@onera.fr.
‡Research Engineer, DAAA, cyril.polacsek@onera.fr.
§Research Engineer, DAAA, daniel-ciprian.mincu@onera.fr.
¶Research Engineer, DAAP, sebastien.deck@onera.fr.

II. Model

A. Boltzmann equation

In a standard CFD solver where the Navier-Stokes equations are solved, the governing equations describe the evolution of macroscopic values (pressure, density, velocity, temperature, ...), whereas in the Boltzmann equation, a mesoscopic description (kinetic energy, momentum, probability of collision between particles) is used. The general governing equation writes

$$\frac{\partial f(\mathbf{x},t,\mathbf{c})}{\partial t} + c_i \frac{\partial f(\mathbf{x},t,\mathbf{c})}{\partial x_i} = \left(\frac{\partial f(\mathbf{x},t,\mathbf{c})}{\partial t}\right)_{\text{coll}}, \tag{1}$$

where $f(\mathbf{x},t,\mathbf{c})$ is the distribution function which represents the density of particles at point $\mathbf{x}$, time t, with a velocity $\mathbf{c}$. The collision term, denoted as $(\partial f(\mathbf{x},t,\mathbf{c})/\partial t)_{\text{coll}}$ in Equation (1), represents the rate of variation which redistributes the energy between particles. From the H-theorem [9], one can see that the collision term describes the tendency of the distribution function $f(\mathbf{x},t,\mathbf{c})$ to tend to an equilibrium distribution function $f^{\text{eq}}(\mathbf{x},t,\mathbf{c})$, characterized by the Maxwell-Boltzmann distribution

$$f^{\text{eq}}(\mathbf{x},t,\mathbf{c}) = \rho\left(\frac{m}{2\pi k_B T}\right)^{D/2} \exp\left(\frac{-m|\mathbf{c}-\mathbf{u}|^2}{2k_B T}\right), \tag{2}$$

where k_B is the Boltzmann constant, T the temperature, m is the particle mass and D the degree of freedom of the particle.

The Bhatnagar-Gross-Krook (BGK) [**?**] collision term is a popular [1–5] simplified linear approximation of the collision term which states that $f(\mathbf{x},t,\mathbf{c})$ tends to $f^{\text{eq}}(\mathbf{x},t,\mathbf{c})$ in a characteristic time τ, often referred to as relaxation time. It reads

$$\left(\frac{\partial f(\mathbf{x},t,\mathbf{c})}{\partial t}\right)_{\text{coll}} = -\frac{f(\mathbf{x},t,\mathbf{c}) - f^{\text{eq}}(\mathbf{x},t,\mathbf{c})}{\tau}. \tag{3}$$

To improve the robustness and accuracy of the BGK collision term, a variant based on a two-relaxation-time collision term [10] is implemented in this work. Referred to as Dual Relaxation Time (DRT), this method over-relaxes the distribution functions $f(\mathbf{x},t,\mathbf{c})$ towards equilibrium while preserving the conservation of mass and momentum, and to reconstruct the non-equilibrium part through a second-order regularization process [10, 11].

From a Chapman-Enskog expansion, one can retrieve the mass density ρ and the fluid momentum $\rho\mathbf{u}$ from

$$\rho(\mathbf{x},t) = \int_{\Re^3} f(\mathbf{x},t,\mathbf{c})\mathrm{d}\mathbf{c} \qquad \text{and} \qquad \rho\mathbf{u}(\mathbf{x},t) = \int_{\Re^3} \mathbf{c}\, f(\mathbf{x},t,\mathbf{c})\mathrm{d}\mathbf{c}. \tag{4}$$

B. Lattice Boltzmann method

In the present work, the Boltzmann equation is dicretized in 3D in a lattice structure along 19 discrete velocities $\mathbf{c}_\alpha$ [12], as represented in Figure 1. Along each discrete velocity, Equation (1) can be seen as a first-order transport equation with a constant convection velocity. With such discrete velocities, the equilibrium distribution functions $f_\alpha^{\text{eq}}(\mathbf{x},t)$ in each α directions can be obtained using Hermite polynomials [12–14]

$$f_\alpha^{\text{eq}}(\mathbf{x},t) = \rho\omega_\alpha\left(1 + \frac{\mathbf{c}_\alpha\cdot\mathbf{u}}{rT} + \frac{1}{2}\left(\frac{\mathbf{c}_\alpha\cdot\mathbf{u}}{rT}\right)^2 - \frac{|\mathbf{u}|^2}{2rT}\right), \tag{5}$$

with ω_α are the weighted constants associated with the Hermite polynomials and $r = k_B/m$ is the gas constant. Nevertheless, Equation (5) is truncated to the second-order, which introduces a approximation error in $\mathrm{o}(M^3)$, where M is the Mach number, which limits such discretization to Mach number up to 0.4.

For each discrete velocity $\mathbf{c}_\alpha$, the associated density of particles is denotes $f_\alpha(\mathbf{x},t)$, therefore equations (4) can be written

$$\rho(\mathbf{x},t) = \sum_\alpha f_\alpha(\mathbf{x},t) \qquad \text{and} \qquad \rho(\mathbf{x},t)\mathbf{u}(\mathbf{x},t) = \sum_\alpha \mathbf{c}_\alpha f_\alpha(\mathbf{x},t). \tag{6}$$

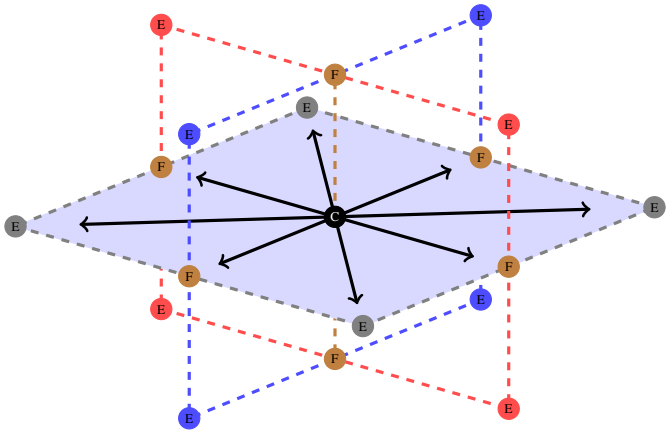

Fig. 1 Representation of the particle velocities $\mathbf{c}_\alpha$ at each node of the D3Q19 lattice. The black node (C) points to the center of the lattice, the brown nodes (F) point to the faces of the neighboor cubes and the blue (E) and red nodes (E) point to the edges of the neighboor cubes. For clarity, only the velocities in the horizontal plane ( ) are displayed.

C. Spalart-Allmaras turbulence model

To correctly simulate the turbulent eddy viscosity ν_t, a fine grid is required near solid boundaries, however, with meshes composed of regular hexahedron elements, it quickly becomes too computationally expensive. To overcome this difficulty, the eddy viscosity can be modeled using a turbulence model, reducing the requirements on the mesh size. In this work, a DDES model [6] based on the Spalart-Allmaras turbulence model [7, 8] is implemented. This model is originally based on the Spalart-Allmaras [7, 8] RANS model which solves one transport equation for a eddy viscosity like variable $\tilde{\nu}$. For clarity, the transition terms are omitted and the standard model reads

$$\frac{D\tilde{\nu}}{Dt} = \underbrace{c_{b1}\tilde{S}\tilde{\nu}}_{\text{production}} + \underbrace{\frac{1}{\sigma}\left[\Delta\cdot((\nu+\tilde{\nu})\Delta\tilde{\nu}) + c_{b2}(\Delta\tilde{\nu})^2\right]}_{\text{diffusion}} - \underbrace{c_{\omega1}f_\omega\left(\frac{\tilde{\nu}}{d_\omega}\right)^2}_{\text{destruction}}. \tag{7}$$

The turbulent eddy viscosity is then recovered via

$$\nu_t = \tilde{\nu} f_{v1}, \tag{8}$$

where the damping term f_{v1} is defined as

$$f_{v1} = \frac{\chi^3}{\chi^3 + c_{v1}^3} \quad \text{with} \quad \chi = \frac{\tilde{\nu}}{\nu}. \tag{9}$$

In the destruction term of Equation (7), the function f_ω allows for a fast decay outside the boundary layer region, and is defined as

$$f_\omega(g) = g\left(\frac{1+c_{\omega3}^6}{g^6+c_{\omega3}^6}\right)^{(1/6)} \quad , \quad g = r + c_{\omega2}(r^6 - r) \quad , \quad r = \frac{\tilde{\nu}}{\tilde{S}K^2 d_\omega^2}\,. \tag{10}$$

The distance-like parameter d_ω defines a trigger which switches from this turbulence modeling in the boundary layer to a usual sub-grid scale viscosity in the rest of the simulation, and is defined as

$$d_\omega = \min(d, C_{\text{DES}}\Delta x) \tag{11}$$

where d is the distance to the wall and Δx is the local mesh size.

Finally, the constants of the model are

$$c_{b1} = 0.1355\,, \quad c_{b2} = 0.622\,, \quad \sigma = \frac{2}{3}\,, \quad K = 0.41\,, \quad c_{\omega1} = \frac{c_{b1}}{K^2} + \frac{1+c_{b2}}{\sigma}\,, \quad c_{\omega2} = 0.3\,, \quad c_{\omega3}\,, \quad c_{v1} = 7.1\,. \tag{12}$$

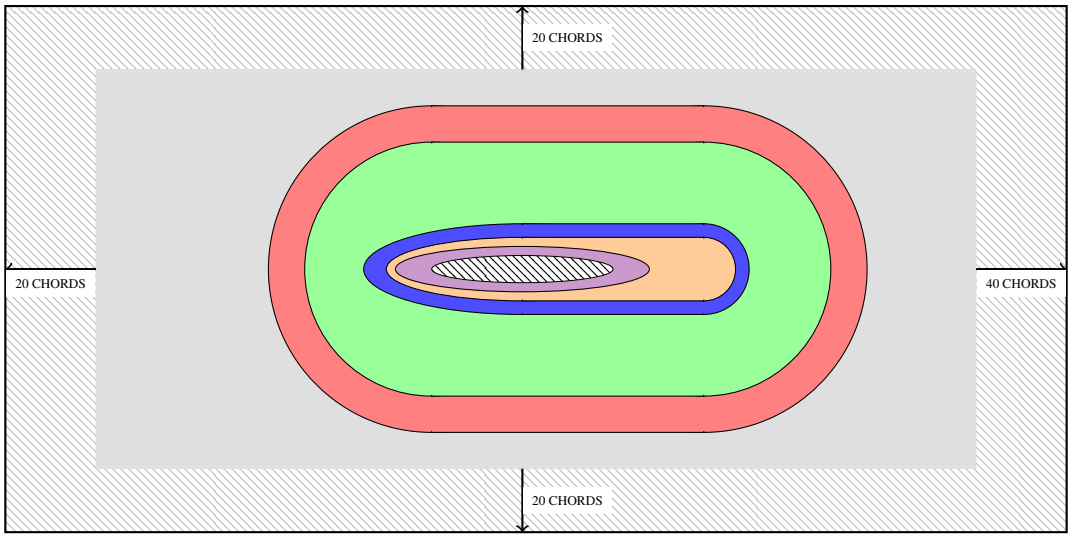

Δt	$5.8.10^{-7}$s	$1.16.10^{-6}$s	$2.32.10^{-6}$s	$4.64.10^{-6}$s	$9.28.10^{-6}$s	$1.86.10^{-5}$s
Δx	$3.5.10^{-4}$m	$7.0.10^{-4}$m	$1.4.10^{-3}$m	$2.8.10^{-3}$m	$5.6.10^{-3}$m	$1.12.10^{-2}$m
Colour						

Fig. 2 Sketch of the mesh strategy of the symmetric aerofoil case. Each embedded colored-box corresponds to a different refinement levels, with the corresponding spatial and time step listed in the table below the sketch.

III. Application to a symmetric aerofoil case

To assess the capability of the turbulence modeling at solid boundaries to properly reproduce boundary layer dynamics at high Reynolds numbers, and therefore self-noise generation, a first benchmark case is studied. It consists in a symmetric NACA0012 aerofoil, at a temperature of 300K, a Mach number of 0.15 and a Reynolds number based on the chord c of the aerofoil of 6 million. The Reynolds number is defined as $\mathrm{Re} = u_\infty L/\nu$ with u_∞ the velocity at infinity, L a characteristic length of the problem, and ν the kinematic viscosity.

This validation case has been extensively studied both numerically and experimentally [15], at different angle of attack (AoA), and is often used to assess the behaviour of a turbulence model [15].

A. Set-up

Based on the Mach number, the Reynolds number and the temperature of the benchmark, if we assume dry air, we can deduce the velocity at infinity $u_\infty = 52.09$m/s, the kinematic viscosity $\nu = 8.7.10^{-6}$ m^2/s and the pressure $P_\infty = 101364$ Pa.

The mesh is composed of 6 levels of refinements, with a ratio of 2 between the mesh size of two adjacent refinement levels. Moreover, in this numerical approach, as the local CFL number is 1 in each grid cell, there is a direct link between the time step and the mesh size of each element. Therefore a multi time step multi mesh size method is used and only the finer elements are computed at each time step. The smallest mesh elements are located at the solid boundary, where the mesh size is $3.5.10^{-4}$ m, which gives a local time step of $5.8.10^{-7}$ s. A sketch of the refinement levels and their associated mesh size/time step used in this work is plotted in Figure 2.

The span of the aerfoil is set to 0.012 m, which correspond to a little over 1% of the chord. To limit blockage effects on the pressure due a restricted domain size, the computational domain extends to 20 chords in all direction except in the downstream direction where the domain extends to 40 chords, as plotted in Figure 2. The final mesh contains approximately 25 million cells. While this is a large number, only a fraction of these elements is computed at each time step (approximately 3 million).

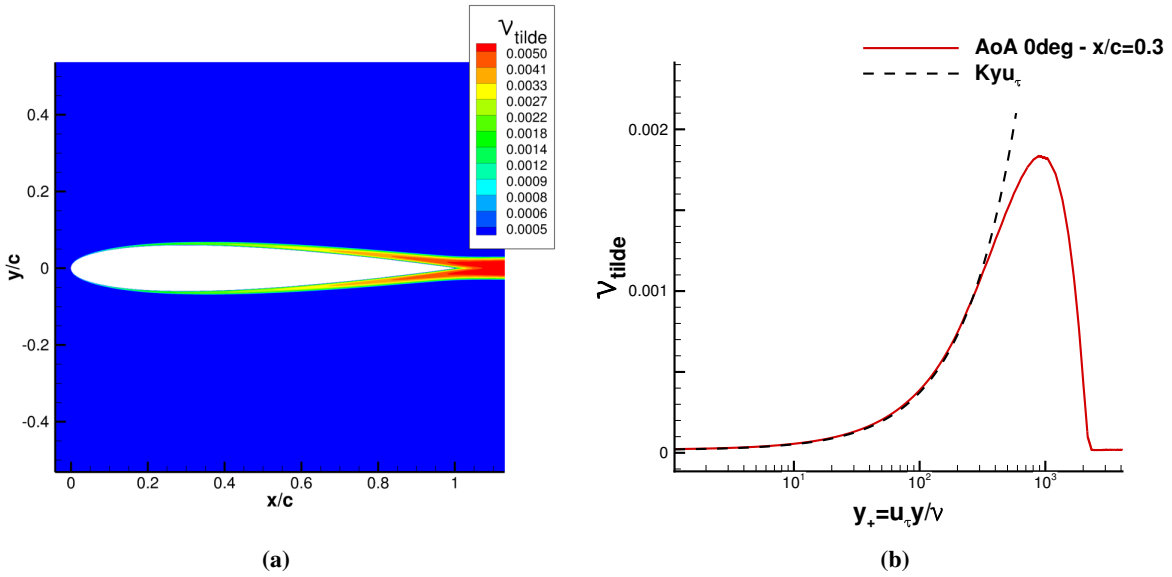

(a) (b)

Fig. 3 (a) Contour of the turbulent eddy viscosity-like $\tilde{\nu}$ around the aerofoil obtained from the Spalart-Allmaras model (b) Evolution of $\tilde{\nu}$ at $x/c = 0.3$ as a function of y_+, along with the linear relation $\tilde{\nu} = Kyu_\tau\nu$ imposed in the Spalart-Allmaras model from the viscous sub-layer to the log-layer via the function f_{v1}.

B. Results

The computation is ran over 5×10^5 iterations, which corresponds to about 0.29 s of simulated time. This equates to the convection of a particle over 15 chords length. Each computation takes about 10h on 128 cores of Intel Nehalem X5560.

At no angle of attack, the evolution of the turbulent eddy viscosity ν_t obtained from the Spalart-Allmaras turbulence model within the simulation is plotted in Figure 3a. Its thickness increases in the chord-wise direction of the aerofoil, which is coherent with the development of a boundary layer where more turbulence implies additional eddy viscosity. Moreover, it displays an expected symmetry between the upper and lower surface. In the Spalart-Allmaras model, the damping function f_{v1} in Equation 9 is defined such that $\tilde{\nu}$ $(= \nu\chi)$ is linear in the viscous sub-layer, the buffer layer and the log-layer, therefore for $y_+(= u_\tau y/\nu)$ up to a few hundreds. This behaviour is verified at multiple locations around the aerofoil, and is plotted for $x/c = 0.3$ on the case with no angle of attack in Figure 3b.

The pressure around the aerofoil, plotted in Figure 4a as the difference between the mean pressure p_0 and the pressure at infinity p_∞, also displays an expected symmetry between the upper and lower surface, which is confirms in Figure 4b by the pressure coefficient C_p defined as

$$C_p = \frac{p - p_\infty}{\frac{1}{2}\rho_\infty u_\infty^2} \,. \tag{13}$$

The maximum pressure, located at the leading edge, is coherent with the physics, with a local pressure coefficient of 1 in the stagnation region. Similarly, as expected, the lowest pressure is observed on the upper and lower surfaces where the velocity experiences the maximum acceleration. Quantitatively and qualitatively, these results in Figure 4b are in very good agreement with the numerical prediction provided within the NASA benchmark [15].

IV. Application to a rod-aerofoil case

Interaction noise is an important aspect of turbomachine noise [1]. In this section, to evaluate this capability, a rod-aerofoil configuration is investigated. It is considered a representative benchmark [16] for numerical modeling of turbulent fluid motions interacting with airframe elements and is recommended by the Advisory Group for Aerospace Research and Development (AGARD). The rod creates a turbulent wake which is convected downstream and impinges the leading edge of the aerofoil. In this case, the boundary layer separation on the rod occurs upstream of the laminar to turbulent transition point which results in fully 3D turbulent structures in the wake. It forms a von Karman vortex

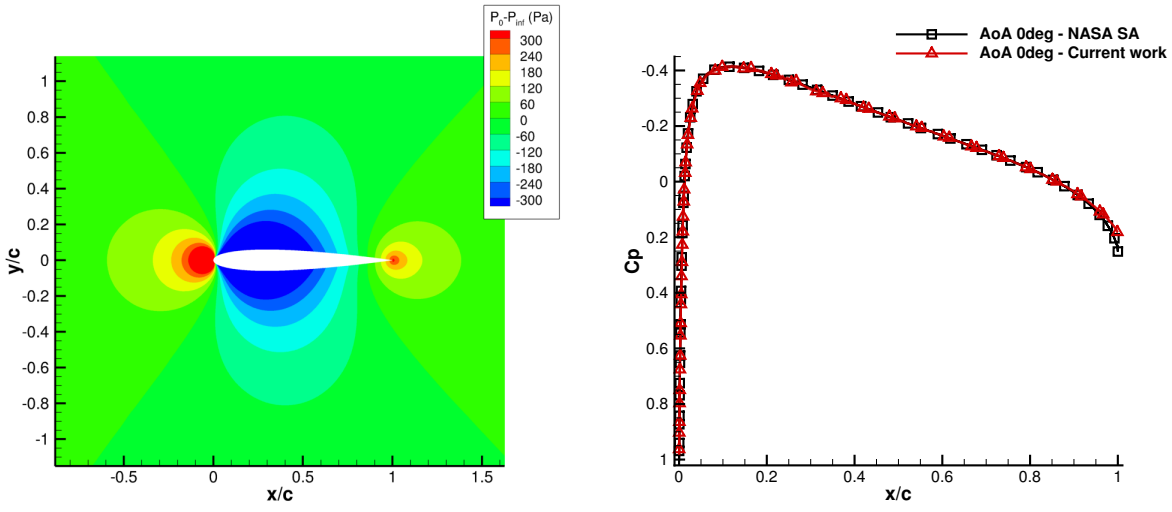

(a) (b)

Fig. 4 (a) Contour of the difference between mean pressure p_0 and the pressure at infinity p_{inf} (b) Pressure coefficient around the aerofoil.

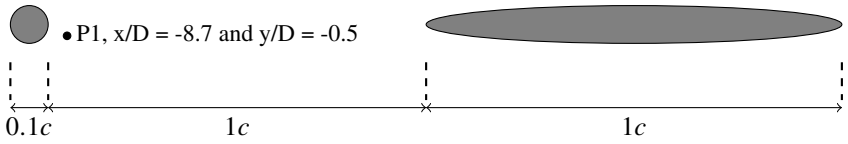

Fig. 5 Dimensions of the rod-aerofoil configuration.

street which creates an asymmetrical pressure distribution around the rod, producing periodic lift variations, therefore generating acoustic perturbations. Similarly, the unsteady lift on the aerofoil created by the incoming turbulence generates leading edge noise which also radiates to the far-field.

A. Set-up

A symmetric NACA0012 aerofoil with a chord c of 0.1 m is placed one chord-length downstream of a rod of diameter $D = 0.1c$, which corresponds to 0.01 m. The situation is depicted in Figure 5. The Reynolds number based on the diameter D of the rod is set to $4.8.10^4$, with an incoming velocity $u_\infty = 72$ m, a temperature $T = 293$ K and a mass density of the fluid $\rho = 1.204$ kg/m^3. The speed of sound is $a_\infty = 343$ m/s giving a Mach number of approximately $M \approx 0.2$.

The mesh is composed of 6 levels of refinements, with a ratio of 2 between the mesh size of two adjacent refinement levels. The smallest mesh elements are located at the solid boundary, where the mesh size is 1.10^{-4} m, which gives a local time step of $1.68.10^{-7}$ s. This corresponds to a wall-distance in wall units, denoted x^+, of about 20. A sketch of the refinement levels and their associated mesh size/time step used in this work is plotted in Figure 6.

B. Results

The computation is ran over 1.2×10^6 iterations, which corresponds to about 0.2 s of simulated time. This equates to the convection of a particle over 140 chords length. Each computation takes about 30h on 280 cores of Intel Xeon Broadwell E5-2680v4.

In Figure 7, a snapshot of the iso-surface of the Q-criterion colored by the streamwise velocity is plotted. It shows the boundary layer separation on the rod, creating a turbulent wake which visibly oscillates at a specific frequency, forming von Karman vortex streets. Then, the turbulent structures of the rod wake impinge the leading edge of the aerofoil, distorting the shape and sizes of these structures.

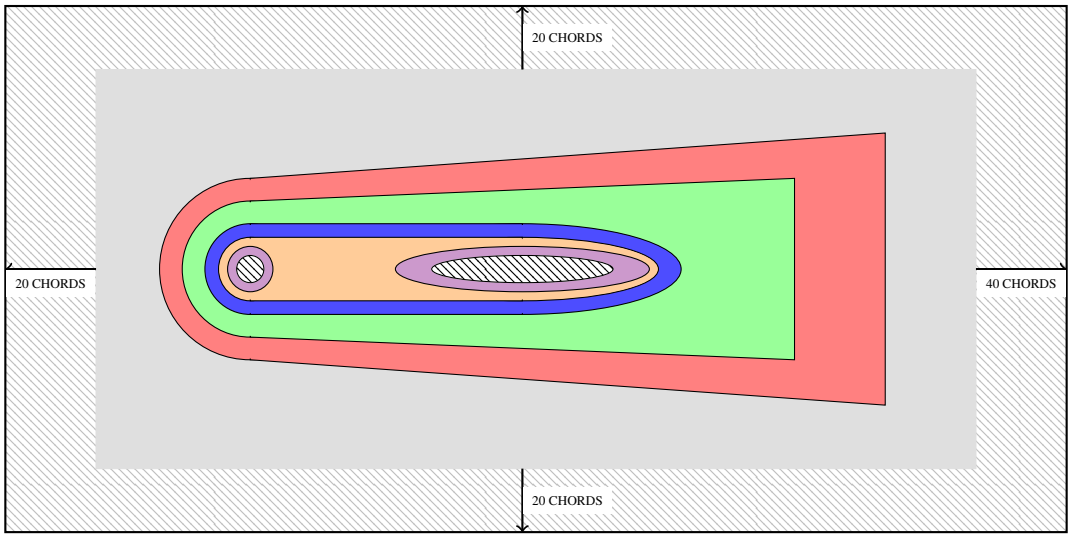

Δt	$1.68.10^{-7}$s	$3.36.10^{-7}$s	$6.73.10^{-7}$s	$1.35.10^{-6}$s	$2.69.10^{-6}$s	$5.38.10^{-6}$s
Δx	$1.0.10^{-4}$m	$2.0.10^{-4}$m	$4.0.10^{-4}$m	$8.0.10^{-4}$m	$1.6.10^{-3}$m	$3.2.10^{-3}$m
Color						

Fig. 6 Sketch of the mesh strategy of the rod-aerofoil case. Each embedded colored-box corresponds to a different refinement levels, with the corresponding spatial and time step listed in the table below the sketch.

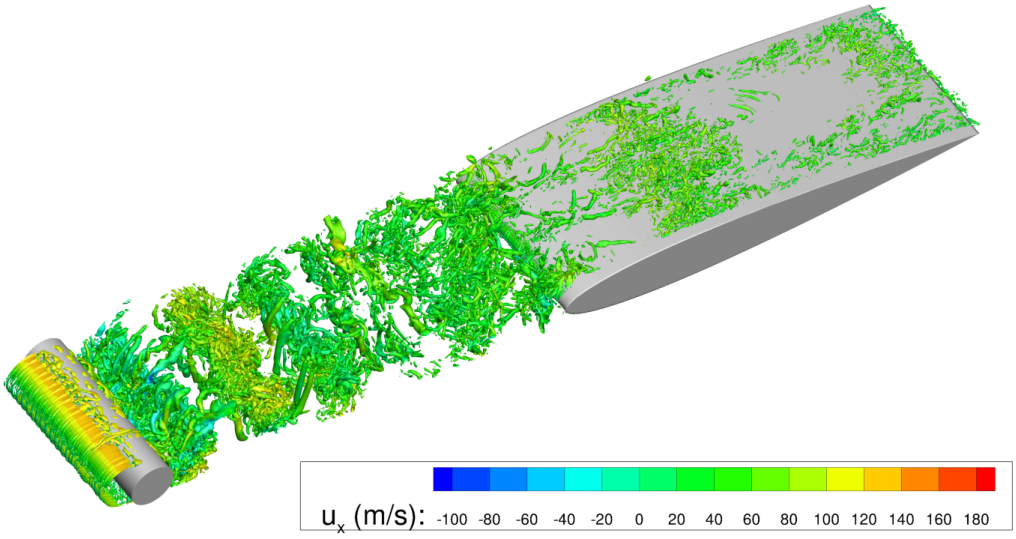

Fig. 7 Iso-surface of the Q-criterion colored by the streamwise velocity in m/s.

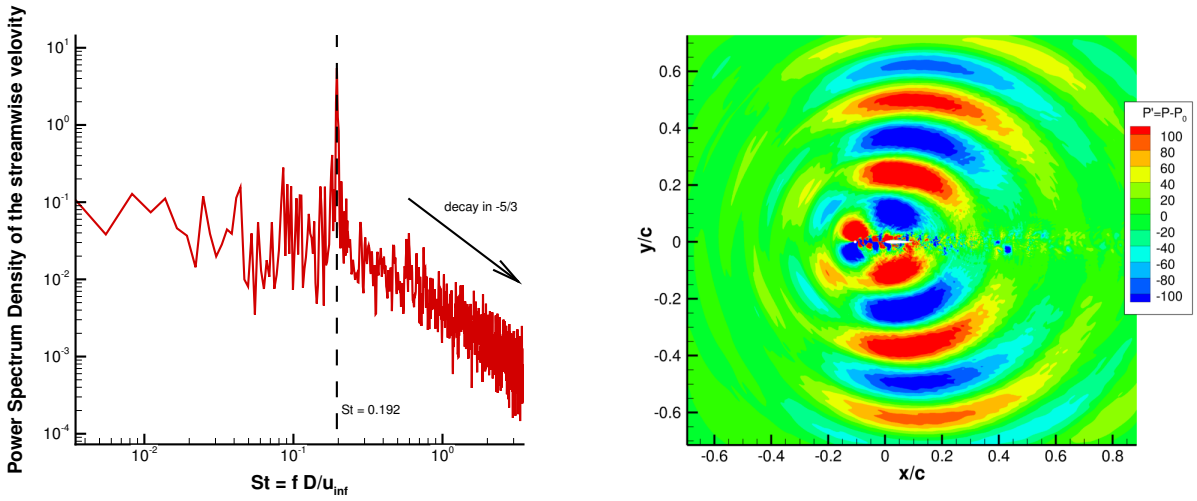

(a) (b)

Fig. 8 (a) Strouhal number as a function of the power spectral density of the streamwise velocity at point P1 in the wake of the rod (b) Contour plot of the unsteady pressure perturbations in the simulation domain.

At a point P1, located downstream of the rod, inside the rod wake (see Figure 5), the unsteady macroscopic values are recorded to perform a spectral analysis on the wake characteristics. The Power Spectral Density (PSD) on the streamwise velocity plotted in Figure 8a depicts a dominant oscillation at a Strouhal number* of $S_t = 0.192$, which is in a very good agreement with experiments [17] and other numerical approaches [18]. Moreover, the high frequency part of the spectrum displays an expected Kolmogorov behaviour for the kinetic energy with a decay slope of -5/3.

The unsteady lift on the aerofoil surface generated by the wake interaction, produces an unsteady acoustic pressure which radiates to the far-field, as visible on the contour plot of the unsteady pressure in Figure 8b. From the Strouhal number of the vortex streets in the wake, the frequency of the acoustic perturbations are approximately 1380Hz, which results in a wavelength in the transverse direction of about $2.5c$, which is in agreement with the unsteady pressure. The wavelength of these oscillations is large with respect to the chord of the aerofoil, therefore it radiates as a dipole. However, an interference pattern is visible in Figure 8b and originates from the unsteady lift on the rod, which also generates acoustical perturbations at the same frequency. These two acoustical sources being separated by a distance different than the wavelength, the two sources radiate with a shifted phase, creating interference patterns. Furthermore, in the far-field, the acoustic perturbations seem to travel unaffected by the change of mesh refinement and do not show any blocking effect due to a restricted domain size.

Finally, the mean pressure coefficients on the rod and on the aerofoil are plotted in Figure 9a and Figure 9b. As expected, they are perfectly symmetric. There is a good agreement with respect to the finite-volume Navier-Stokes LES (AVBP). Note that in this reference case, the LES is wall-resolved, therefore it does not rely on a turbulence model at the surface.

V. Application to a mobile turbofan engine case

With the objective of simulating complex turbofan applications, a more representative test-case which combines self-noise and interaction noise on mobile surfaces is investigated using a turbofan in rotation interacting with a grid-generated incoming turbulence.

A collaboration with Thomas Carolus of the University of Siegen is being set-up to perform experiments on this configuration. It will likely be based on a geometry already experimentally studied [19] but for self-noise, and will therefore be extended to consider interaction noise. A similar case has been studied experimentally [20] and their set up is described in Figure 10.

This case is currently being set up in our solver, therefore there are no result yet.

*Strouhal number $S_t = \frac{fL}{u_\infty}$ where L is a characteristic length of the problem

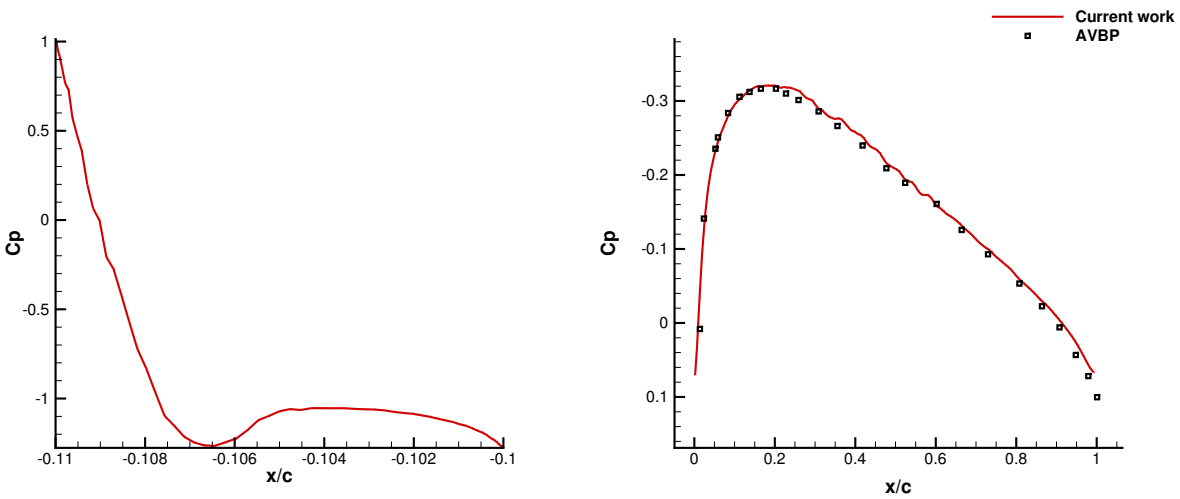

Fig. 9 Mean pressure coefficient (a) on the rod and (b) on the aerofoil.

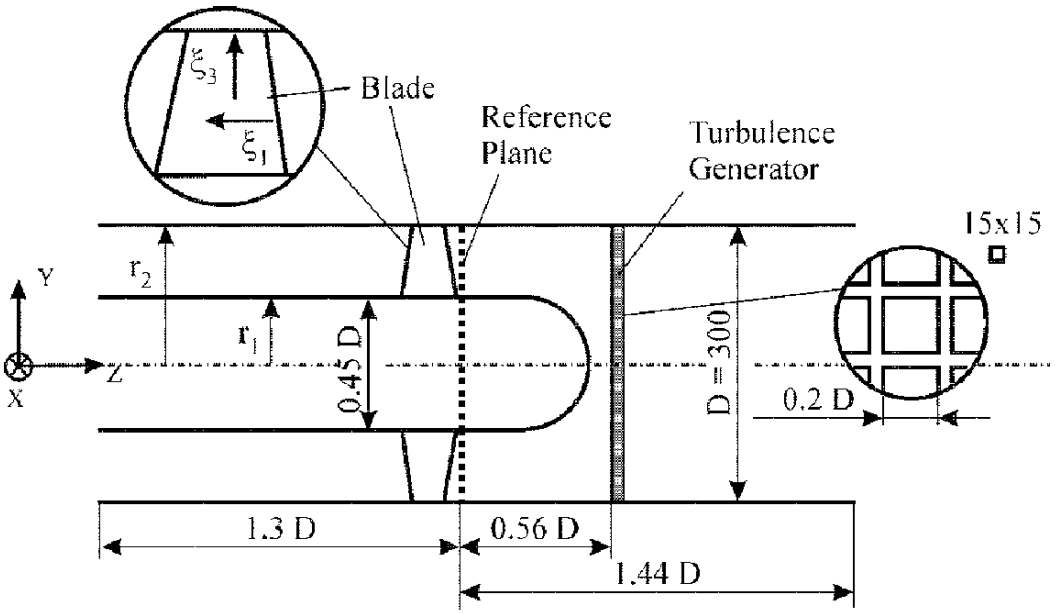

Fig. 10 Experimental set up of the interaction noise from a rotating fan impinged by a grid-generated turbulence. In this representation, the flow travels from right to left. Reproduced from [20]

VI. Content of the full paper

The full paper will include

- a more detailed description of the numerical implementation of the DDES approach used in this work
- regarding the NACA0012 aerofoil case, multiple angles of attack, including a separation case, will be investigated
- a more comprehensive analysis of the rod-aerofoil case, with comparison with experiments and other numerical approaches of the separation bubble behind the rod, the RMS pressure coefficients of the rod/aerofoil, the velocity profiles at different locations, ... Also, it will include a comparison of the direct far-field against porous and solid Ffowcs Williams and Hawkings analogy
- regarding the turbofan engine case, it will include the set-up, a detailed aerodynamic and aeroacoustic analysis, with comparisons with experiments.

References

[1] Khorrami, M. R., Fares, E., and Casalino, D., "Towards full aircraft airframe noise prediction: lattice Boltzmann simulations," *AIAA Paper*, Vol. 2481, 2014, p. 2014.

[2] Sengissen, A., Giret, J.-C., Coreixas, C., and Boussuge, J.-F., "Simulations of LAGOON landing-gear noise using Lattice Boltzmann Solver," *21st AIAA/CEAS Aeroacoustics Conference*, 2015, p. 2993.

[3] Romani, G., and Casalino, D., "APPLICATION OF LATTICE-BOLTZMANN METHOD TO ROTORCRAFT AERODYNAMICS AND AEROACOUSTICS," 2017.

[4] Barad, M. F., Kocheemoolayil, J. G., and Kiris, C. C., "Lattice Boltzmann and Navier-Stokes Cartesian CFD Approaches for Airframe Noise Predictions," *23rd AIAA Computational Fluid Dynamics Conference*, 2017, p. 4404.

[5] Shin, Y., Polidoro, F., Gonzalez-Martino, I., and Casalino, D., "Aircraft Cabin Outflow Valve Tonal and Broadband Noise Prediction Using the Lattice Boltzmann Method," *23rd AIAA/CEAS Aeroacoustics Conference*, 2017, p. 3359.

[6] Spalart, P. R., Deck, S., Shur, M., Squires, K., Strelets, M. K., and Travin, A., "A new version of detached-eddy simulation, resistant to ambiguous grid densities," *Theoretical and computational fluid dynamics*, Vol. 20, No. 3, 2006, pp. 181–195.

[7] Spalart, P. R., and Allmaras, S. R., "A One-Equation Turbulence Model for Aerodynamic Flows," *AIAA Paper*, Vol. 92, 1992, p. 0439.

[8] Spalart, P. R., Allmaras, S. R., et al., "A one equation turbulence model for aerodynamic flows," *RECHERCHE AEROSPATIALE-FRENCH EDITION-*, 1994, pp. 5–5.

[9] Boltzmann, L., "Weirere Studien uber das warmegleich-gewich unter gasmolekulen," *K. Acad. Wiss.(Wein) Sitzb., II Abt*, Vol. 66, 1872.

[10] Ricot, D., Marié, S., Sagaut, P., and Bailly, C., "Lattice Boltzmann method with selective viscosity filter," *Journal of Computational Physics*, Vol. 228, No. 12, 2009, pp. 4478–4490. doi:10.1016/j.jcp.2009.03.030, URL `http://dx.doi.org/10.1016/j.jcp.2009.03.030`.

[11] Latt, J., and Chopard, B., "Lattice Boltzmann method with regularized pre-collision distribution functions," *Mathematics and Computers in Simulations*, Vol. 72, 2006, pp. 165–168. doi:10.1016/j.matcom.2006.05.017.

[12] He, X., Shan, X., and Doolen, G. D., "Discrete Boltzmann equation model for nonideal gases," *Physical Review E*, Vol. 57, No. 1, 1998, pp. 13–16.

[13] Grad, H., "Note on N-dimensional hermite polynomials," *Communications on Pure and Applied Mathematics*, Vol. 2, No. 4, 1949, pp. 325–330.

[14] Grad, H., "On the kinetic theory of rarefied gases," *Communications on pure and applied mathematics*, Vol. 2, No. 4, 1949, pp. 331–407.

[15] Dennis, J., Thomas, P., and Marissa, C., "OVERFLOW Turbulence Modeling Resource Validation Results," Tech. Rep. NAS-2016-01, NASA, 2016.

[16] Jiang, Y., Mao, M.-L., Deng, X.-G., and Liu, H.-Y., "Numerical investigation on body-wake flow interaction over rod–airfoil configuration," *Journal of Fluid Mechanics*, Vol. 779, 2015, pp. 1–35.

[17] Jacob, M. C., Boudet, J., Casalino, D., and Michard, M., "A rod-airfoil experiment as a benchmark for broadband noise modeling," *Theoretical and Computational Fluid Dynamics*, Vol. 19, No. 3, 2005, pp. 171–196.

[18] Touil, H., Bazin, B., J.-C. Giret and, S. M., Lévêque, E., Boudet, J., Ricot, D., and Sengissen, A., "Large-eddy simulation of rod-airfoil flow configuration in the subcritical turbulent regime by using the lattice Boltzmann method," *52 nd 3AF International Conference on Applied Aerodynamics*, 2017.

[19] Carolus, T., Zhu, T., and Sturm, M., "A low pressure axial fan for benchmarking prediction methods for aerodynamic performance and sound," *FAN2015-International Conference on Fan Noise, Technology and Numerical Methods, Lyon, France*, 2015.

[20] Reese, H., Kato, C., and Carolus, T. H., "Large eddy simulation of acoustical sources in a low pressure axial-flow fan encountering highly turbulent inflow," *Journal of fluids engineering*, Vol. 129, No. 3, 2007, pp. 263–272.